I&EC research
Industrial & Engineering Chemistry Research
pubs.acs.org/IECR

Article

Thymol-Based Natural Deep Eutectic Solvents under Pressure: A Novel Platform for Green Solvents

Ozge Ozkilinc, Alfredo Bol-Arreba, Miguel Angel Soler, Federico Fogolari,* and Santiago Aparicio*

Cite This: *Ind. Eng. Chem. Res.* 2025, 64, 17958−17974

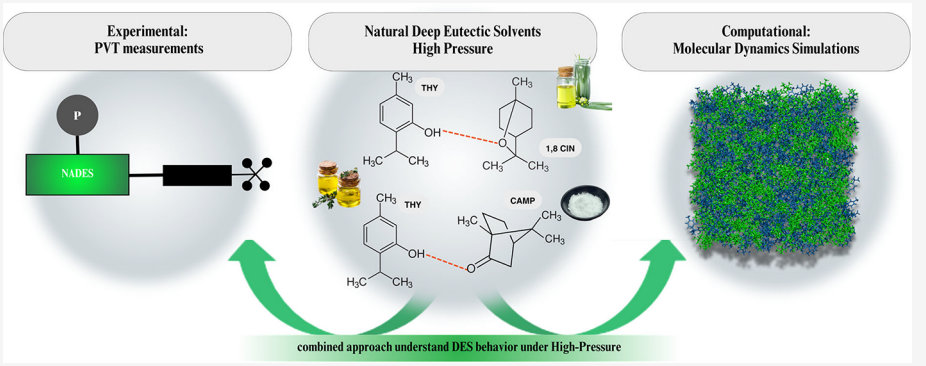

ABSTRACT: Deep eutectic solvents (DESs) are emerging green alternatives to traditional solvents, yet their behavior under high pressure (HP) remains underexplored. This study examines two thymol-based eutectic mixtures—thymol:1,8-cineole (1:1) and thymol:camphor (1:1)—using a combined experimental and molecular dynamics approach. Pressure−volume−temperature (PVT) measurements were conducted across 0.1−60 MPa and 293.15−343.15 K. The two systems displayed expected density trends but exhibited markedly different internal pressure responses: a maximum for the camphor system and a shallow minimum for the cineole mixture. Molecular dynamics simulations revealed more frequent hydrogen bonding and greater structural organization in the camphor system, highlighting how molecular structure affects interactions. Changes in hydrogen bonding and internal pressure remained within 25% over the entire pressure range. These results provide molecular-level insight into pressure effects on DESs, guiding their future application in chemical processing and materials science under nonambient conditions.

1. INTRODUCTION

In the last 20 years, research and innovation in environmentally friendly solvents have increased, motivated by the worldwide focus on sustainability and the preservation of the environment.[1] This shift has been significantly influenced by calls from global organizations like the United Nations (UN), which advocate for sustainable development and the reduction of harmful environmental impacts.[2] Deep eutectic solvents (DESs) were introduced in 2003[3] as a class of green solvents formed by a mixture of compounds consisting of a hydrogen bond donor and a hydrogen bond acceptor, resulting in a eutectic point with a lower melting point than the individual components.[4] Unlike traditional solvents, which can be toxic and harmful to the environment, DESs are generally biodegradable and less toxic. Additionally, their properties can be tailored for specific applications by adjusting the type and ratio of the components.[5]

DESs are classified into five types based on the nature of their components: Type I DESs are composed of a quaternary ammonium salt and a metal chloride, while Type II DESs include a quaternary ammonium salt and a metal chloride hydrate. The most common type, Type III DESs, comprise a quaternary ammonium salt and a hydrogen bond donor (HBD) such as a carboxylic acid, sugar, or alcohol. Type IV DESs are formed from a metal chloride hydrate and a HBD.[6] Type V DESs, which have been the last to be introduced, are composed of two nonionic compounds. They are formed by the interaction between a HBD, often a phenolic compound, and a hydrogen bond acceptor (HBA) molecule.[7] As a result, they have lower viscosities compared to their ionic counterparts.[8,9] The low viscosity of Type V DESs facilitates faster mass transfer, which is crucial for the efficient dissolution of organic and inorganic compounds in industrial applications. In contrast, hydrophilic DESs have higher viscosity and slower

Received: January 8, 2025
Revised: August 25, 2025
Accepted: August 27, 2025
Published: September 1, 2025

https://doi.org/10.1021/acs.iecr.5c00116
Ind. Eng. Chem. Res. 2025, 64, 17958−17974

mass transfer rates, limiting their efficiency in industrial processes. This lower viscosity makes Type V DESs promising candidates for a variety of industrial applications.[10] Another subcategory of DESs are Natural deep eutectic solvents (NADESs) where both the HBD and HBA are derived from natural sources.[11] This contributes to the development of environmentally friendly and sustainable solvents that exhibit biodegradability and low toxicity.[12] NADESs frequently have specific functional groups that improve their selectivity toward certain solutes, rendering them particularly appealing for biobased applications.[13,14] Additionally, deep eutectic solvents are categorized into hydrophobic and hydrophilic types.[15] Hydrophobic DESs are especially valuable for solubilizing poorly water-soluble compounds, which is highly relevant for pharmaceutical and environmental applications.[16]

From a chemical engineering perspective, the sustainability of these solvents depends on several key factors. To enhance processability, it is essential to minimize the viscosity of the DES. Low-viscosity solvents facilitate easier handling and reduce the energy required for mixing and separation. Additionally, maximizing the density difference between the DES and water is crucial. A larger density difference significantly improves the macroscopic phase separation process, making it more energy efficient. This efficiency is vital for the sustainable application of DESs, as it directly impacts the energy demands of separation processes.[17,18] A particular area of DESs application which is scarcely studied stands on the use of DESs for High Pressure (HP) operations. Understanding the behavior of DESs under HP conditions is crucial for optimizing their performance in various applications. Pressure significantly influences the physicochemical properties of DESs, affecting density, viscosity, conductivity, and phase transitions due to changes in liquid structuring and intermolecular forces under compression. Therefore, Pressure−volume−temperature (PVT) studies are essential for characterizing the thermodynamic properties of DESs and predicting their behavior in various HP applications. Utilizing pressure swing designs, CO_2 can be efficiently captured and released, significantly reducing the costs of carbon capture operations.[19] Recently, DESs have also been studied as high-performance lubricants under 2.16 GPa.[20,21]

Previous studies have revealed that, as expected, applying HP to DESs often leads to a decrease in their molar volume and an increase in their density and viscosity. These changes can significantly affect their solvating ability and transport properties. This work presents a comprehensive experimental and computational investigation into the behavior of archetypical type V NADESs, thymol (THY) + 1,8-cineole (CIN) and thymol + camphor (CAMP), both in a 1:1 mol ratio − under HP conditions. The experimental viscosity data for these NADES being 25.1 and 20.817 mPa s at 293.15 and 298.15 K for THY:CIN and THY:CAMP (1:1), respectively,[9,22] confirms that these are low viscous NADES. Regarding the safety and sustainability, a previous study[9] has reported some minor toxicity problems such as eye irritation but discarding other relevant toxicity effects. Likewise, although some aquatic (fish) toxicity is inferred, the considered materials are biodegradable, and thus they may be considered as mostly safe. Likewise, the components of the NADES[9] may be produced from renewable sources at low cost, thus ensuring the sustainability of production processes. The research integrates experimental and computational methods, focusing experimentally on characterizing the pressure−volume−temperature (PVT) behavior of the selected NADESs using advanced HP techniques. Computationally, classical molecular dynamics simulations are employed to provide detailed insights into the microscopic interactions and structural organization of NADESs under HP, with a specific emphasis on the dynamic changes in intermolecular hydrogen bonding, which crucially influence their fluidic properties. By synergistically combining these two approaches, this study aims to deepen our understanding of how intermolecular forces govern the nanostructuring and evolution of NADESs under compression.

2. MATERIALS AND METHODS

2.1. Experimental PVT Studies. The pure compounds used for NADES preparation: THY (CAS: 89−83−8, purity 99.5%), CIN (CAS: 470−82−6, purity 99%) and CAMP (76−22−2, purity 99.0%), were obtained from MERCK and used without further purification. THY:CIN and THY:CAMP, both in 1:1 mol ratio, NADES (Figure 1a) were prepared by mixing suitable amounts (weighed with Mettler AT261 balance, $\pm 1 \cdot 10^{-5}$ g) of each compound, which were placed into closed glass flasks and stirred for 12 h while heating at 313 K. Liquid, colorless and transparent phases were formed (without traces of turbidity), which were dried under vacuum (Heidolph

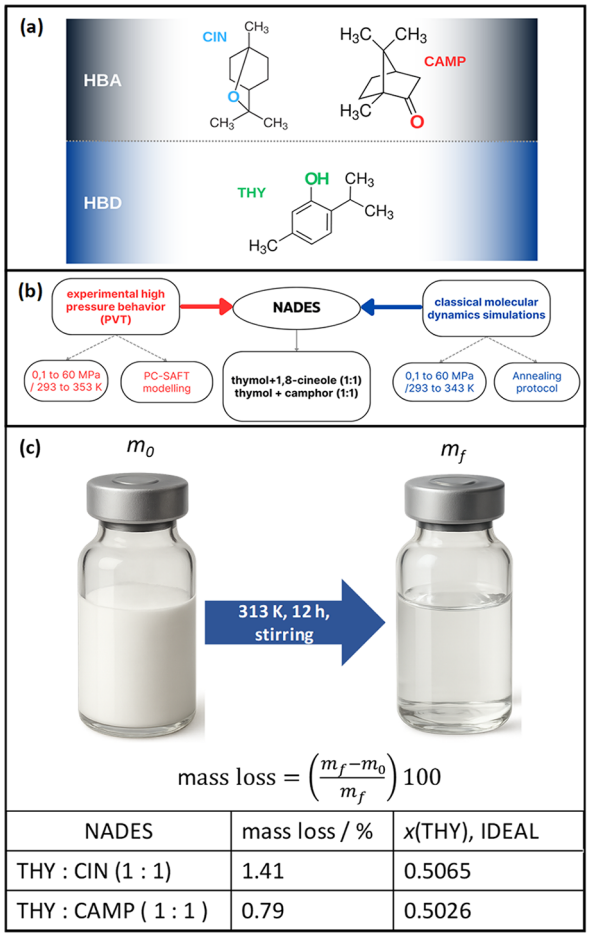

NADES	mass loss / %	x(THY), IDEAL
THY : CIN (1 : 1)	1.41	0.5065
THY : CAMP (1 : 1)	0.79	0.5026

Figure 1. (a) Molecular structures of compounds used in this work for NADES preparation, (b) methodology considered in this work, (c) scheme of methodology used for determining possible preferential evaporation during the NADES preparation procedure and calculated final NADES composition considering mass loss and ideal mixture behavior.

https://doi.org/10.1021/acs.iecr.5c00116
Ind. Eng. Chem. Res. 2025, 64, 17958−17974

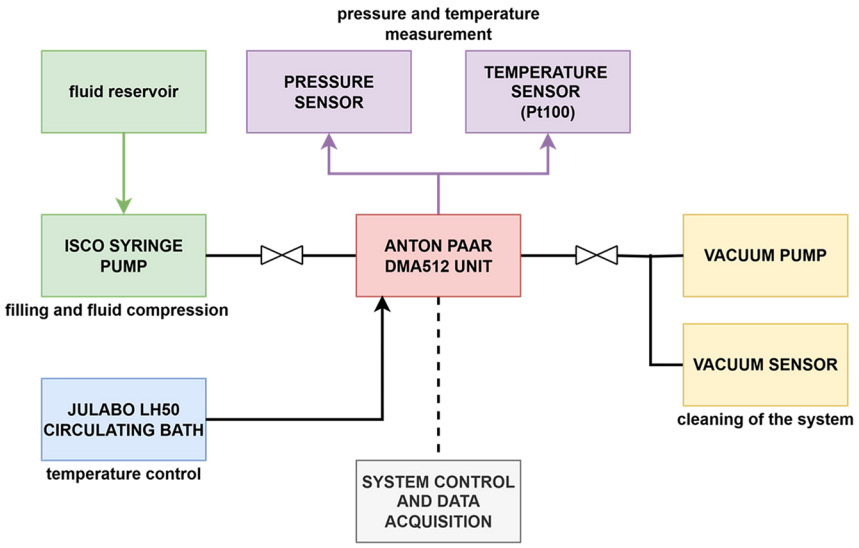

Figure 2. Schematic diagram of the high-pressure vibrating tube densimeter setup used for PVT measurements. The system consists of an ISCO syringe pump for pressure control, a DMA 512P vibrating tube densimeter with the vibrating tube thermostated with a Julabo LH50 bath for temperature regulation, and a DMA 58 digital densimeter connected to a data acquisition system for real-time monitoring. Pressure is monitored via an integrated pressure transducer. The sample is injected into the densimeter, and its oscillation period is used to compute fluid density.

rotary evaporator) also at 313 K for 24 h. The water content of the samples was measured (Karl Fischer coulometric titrator, Metrohm 831 KF coulometer), showing 0.11 and 0.09 wt % for THY:CIN (1:1) and THY:CAM (1:1), respectively. The reported water content is reasonably low, having negligible effect(s) on NADES properties,[23] and thus no further drying was considered. The prepared NADES were kept in sealed flasks, remaining liquid at 293 K without traces of turbidity in the period of study (three months). The differences in volatilities among the components of the considered NADES may lead to questions about the possible relative evaporation, and thus to the changes in NADES composition with regard to the stated 1:1 NADES. The literature vapor pressures for the involved components are 12.7 Pa (at 313.15 K), 627 Pa (at 313.15) and 59.89 Pa (at 308.15 K),[24−26] for THY, CIN and CAMP, respectively, which indicate low evaporation at the considered preparation temperature (313 K). Nevertheless, the effect of relative evaporation was quantified, Figure 1c. Samples were weighed just upon the addition of the two corresponding compounds (m_0) and after the 12 h period at 313 K (m_f), thus obtaining the evaporation loss in the considered closed vessels. From that the final composition of the formed NADES was calculated considering ideal behavior, leading to x(THY) = 0.5065 for THY:CIN and x(THY) = 0.5026 for THY:CAMP, both supposed as x(THY) = 0.5000, i.e. 1.30 and 0.52% differences in the stated mole fractions, respectively, which would be the corresponding errors for the NADES composition. Therefore, the changes in NADES composition are very minor during the preparation procedure, and mixtures (NADES) may be considered as equimolar. No density data was found in the literature for THY:CIN (1:1) but for THY:CAMP (1:1) Abdallah et al.[27] reported a value of 0.9675 g cm^{-3} at 298.15 K and ambient pressure, which is only −0.22% lower than the value obtained in this work (0.9697 g cm^{-3}, at the same conditions 1 bar). Likewise, the NADES preparation procedure reported in[27] considers mixing components at 363 K, much higher temperature than the one considered in this work.

Experimental density−temperature−pressure (PVT) studies were carried out using a HP apparatus around a vibrating tube densimeter.[28] This setup has been proven effective for measuring fluids with properties similar to deep eutectic solvents (DES), such as ionic liquids (ILs)[29] and applied in a previous study on PVT behavior of NADES.[30] The scarcity of existing literature on (NA)DES PVT properties further supports the suitability of this approach, with several studies utilizing vibrating tube devices.[31−34] A schematic diagram of the high-pressure vibrating tube densimeter setup used in this study is provided in Figure 2. The apparatus is based on the Anton Paar DMA512P vibrating U-tube cell integrated with a DMA58 digital densimeter, with temperature control achieved via a Julabo LH50 thermostatic bath and pressure regulated by a Teledyne ISCO 100DM syringe pump. Temperature and pressure were measured using calibrated Pt100 thermometers and a high-accuracy pressure transducer, respectively, each with uncertainties of ±0.01 K and ±0.01 MPa. The oscillation period of the vibrating tube was recorded with a resolution of 0.01 μs, and the calibration of the densimeter was performed using Milli-Q water and n-hexane as reference fluids, following established protocols.[28] Calibration was carried out using Millipore Milli-Q water (resistivity 18.2 MΩ cm) and n-hexane (Merck, 99.9% purity) as reference fluids, with their density data obtained from established literature sources.[35,36] The working equation relating vibrating period to density was the 14-parameter equation established by Ihmels et al.[37] Through an error analysis, the density uncertainty was determined to be ±0.0001 g cm^{-3}.[38]

The PVT data, Table 1, was fitted to eq 1, with the fitting coefficients reported in Table 2, which was used to calculate relevant derived thermophysical properties: thermal expansion coefficient, α_p, isothermal compressibility, κ_T, and internal pressure, P_i, using the corresponding thermodynamic relationships (eqs 2−4).[39]

$$\rho = a_{00} + a_{10}T + a_{01}p + a_{20}T^2 + a_{11}Tp + a_{02}p^2 + a_{30}T^3 + a_{21}T^2p + a_{12}Tp^2 + a_{03}p^3 \quad (1)$$

https://doi.org/10.1021/acs.iecr.5c00116
Ind. Eng. Chem. Res. 2025, 64, 17958−17974

Table 1. Results for the Studied NADES Reporting Experimental Properties as a Function of Pressure and Temperature[a,b]

		ρ/g cm^{-3}	$10^3\ \alpha_P$/K^{-1}	κ_T/TPa^{-1}	P_i/MPa	ρ/g cm^{-3}	$10^3\ \alpha_P$/K^{-1}	κ_T/TPa^{-1}	P_i/MPa
T/K	P/MPa	THY:CIN (1:1)				THY:CAMP (1:1)			
293.15	1.0	0.9625	0.817	508.0	470.4	0.9735	0.657	618.1	310.8
303.15	1.0	0.9547	0.831	535.4	469.7	0.9669	0.669	622.2	324.8
313.15	1.0	0.9468	0.843	564.8	466.6	0.9605	0.676	626.0	337.0
323.15	1.0	0.9388	0.853	596.1	461.4	0.9541	0.679	629.6	347.3
333.15	1.0	0.9309	0.860	629.4	454.1	0.9479	0.677	632.9	355.3
343.15	1.0	0.9230	0.864	664.8	444.9	0.9414	0.671	636.3	361.0
353.15	1.0	0.9150	0.865	702.4	434.1	0.9355	0.661	639.1	364.0
293.15	5.0	0.9641	0.807	515.9	453.4	0.9766	0.655	589.6	320.7
303.15	5.0	0.9563	0.820	542.6	453.4	0.9699	0.666	595.4	334.3
313.15	5.0	0.9484	0.832	571.3	451.0	0.9637	0.673	600.7	346.0
323.15	5.0	0.9404	0.841	602.0	446.3	0.9572	0.676	606.1	355.6
333.15	5.0	0.9324	0.847	634.6	439.6	0.9506	0.675	611.4	362.8
343.15	5.0	0.9245	0.850	669.3	431.0	0.9438	0.670	616.6	367.6
353.15	5.0	0.9165	0.851	706.1	420.6	0.9378	0.659	621.2	369.7
293.15	10.0	0.9668	0.794	522.9	435.1	0.9792	0.652	558.4	332.2
303.15	10.0	0.9590	0.807	548.8	435.7	0.9729	0.663	566.0	345.1
313.15	10.0	0.9512	0.817	576.5	433.9	0.9663	0.670	573.6	355.9
323.15	10.0	0.9434	0.825	606.1	429.8	0.9598	0.673	581.1	364.4
333.15	10.0	0.9356	0.830	637.8	423.7	0.9537	0.672	588.3	370.4
343.15	10.0	0.9279	0.833	671.3	415.6	0.9465	0.667	596.0	373.9
353.15	10.0	0.9201	0.832	707.0	405.7	0.9406	0.656	602.7	374.5
293.15	20.0	0.9721	0.770	529.0	406.6	0.9842	0.642	508.0	350.6
303.15	20.0	0.9647	0.781	552.8	408.1	0.9774	0.654	520.0	361.1
313.15	20.0	0.9571	0.789	578.6	407.1	0.9714	0.661	531.7	369.2
323.15	20.0	0.9496	0.795	606.2	403.8	0.9650	0.664	543.4	374.8
333.15	20.0	0.9420	0.798	635.7	398.3	0.9585	0.663	555.1	377.7
343.15	20.0	0.9346	0.799	667.1	390.8	0.9520	0.657	566.8	378.0
353.15	20.0	0.9272	0.796	700.4	381.4	0.9461	0.647	578.1	375.4
293.15	30.0	0.9771	0.748	524.5	387.9	0.9883	0.629	473.7	359.1
303.15	30.0	0.9698	0.757	546.5	389.9	0.9824	0.640	489.6	366.1
313.15	30.0	0.9624	0.764	570.3	389.4	0.9764	0.647	505.5	370.7
323.15	30.0	0.9551	0.768	595.9	386.4	0.9702	0.650	521.5	372.7
333.15	30.0	0.9478	0.769	623.2	381.1	0.9638	0.649	537.6	372.1
343.15	30.0	0.9406	0.768	652.4	373.7	0.9578	0.643	553.5	368.9
353.15	30.0	0.9334	0.763	683.5	364.3	0.9515	0.634	569.5	362.9
293.15	40.0	0.9822	0.728	509.6	378.6	0.9941	0.610	454.1	353.7
303.15	40.0	0.9751	0.735	529.6	380.8	0.9878	0.621	474.5	356.9
313.15	40.0	0.9679	0.740	551.3	380.3	0.9815	0.628	494.9	357.7
323.15	40.0	0.9607	0.742	574.8	377.3	0.9750	0.632	515.4	356.1
333.15	40.0	0.9537	0.742	600.0	371.9	0.9689	0.631	535.8	352.1
343.15	40.0	0.9467	0.738	627.0	364.2	0.9627	0.625	556.4	345.8
353.15	40.0	0.9397	0.732	655.9	354.3	0.9571	0.615	576.5	336.9
293.15	50.0	0.9870	0.710	484.6	379.3	0.9982	0.588	450.5	332.5
303.15	50.0	0.9799	0.715	502.6	381.5	0.9922	0.599	475.1	332.2
313.15	50.0	0.9727	0.719	522.3	380.9	0.9861	0.606	499.8	329.7
323.15	50.0	0.9658	0.719	543.7	377.5	0.9806	0.609	524.3	325.3
333.15	50.0	0.9589	0.717	566.7	371.5	0.9743	0.608	549.3	318.7
343.15	50.0	0.9521	0.712	591.5	363.0	0.9686	0.602	574.1	310.1
353.15	50.0	0.9454	0.704	618.0	352.3	0.9631	0.593	598.9	299.4
293.15	60.0	0.9917	0.693	449.4	392.3	1.0026	0.561	461.7	296.3
303.15	60.0	0.9850	0.697	465.3	394.4	0.9968	0.572	490.7	293.6
313.15	60.0	0.9782	0.699	482.8	393.4	0.9911	0.579	519.7	289.0
323.15	60.0	0.9713	0.698	502.0	389.2	0.9859	0.582	548.5	282.8
333.15	60.0	0.9646	0.694	522.9	382.1	0.9797	0.581	578.1	274.8
343.15	60.0	0.9579	0.687	545.4	372.3	0.9742	0.575	607.4	265.1
353.15	60.0	0.9513	0.678	569.7	360.0	0.9683	0.566	637.0	253.7

[a]Uncertainties: 0.0001 g cm^{-3} (ρ); 0.001 K^{-1} ($10^3\ \alpha_P$); 0.1 TPa^{-1} (κ_T); 0.1 MPa (P_i). [b]Density, ρ, thermal expansion coefficient, α_P, isothermal compressibility, κ_T, and internal pressure, P_i.

https://doi.org/10.1021/acs.iecr.5c00116
Ind. Eng. Chem. Res. 2025, 64, 17958−17974

Table 2. Fitting Coefficients of Experimental Density (g cm^{-3}) for the Considered NADES as a Function of Pressure (MPa) and Temperature (K), (Table 1) According to eq 1

parameter	THY:CIN (1:1)	THY:CAMP (1:1)
a00	1.0460	0.9525
a10	0.0004418	0.0005346
a01	0.0005905	0.0013670
a20	$3.584\cdot10^{-6}$	$-9.997\cdot10^{-6}$
a11	$-1.860\cdot10^{-6}$	$5.522\cdot10^{-7}$
a02	$-4.260\cdot10^{-6}$	$-6.417\cdot10^{-6}$
a30	$-1.718\cdot10^{-8}$	$2.502\cdot10^{-8}$
a21	$-8.114\cdot10^{-9}$	$2.228\cdot10^{-8}$
a12	$6.868\cdot10^{-9}$	$-1.023\cdot10^{-9}$
a03	$4.339\cdot10^{-9}$	$6.809\cdot10^{-9}$
goodness of fit		
SSE	$3.192\cdot10^{-6}$	$4.153\cdot10^{-6}$
R^2	0.9998	0.9997
RMSE	0.0003	0.0003

$$\alpha_p = \frac{-1}{\rho}\left(\frac{\partial \rho}{\partial T}\right)_p \tag{2}$$

$$\kappa_T = \frac{1}{\rho}\left(\frac{\partial \rho}{\partial p}\right)_T \tag{3}$$

$$P_i = T\frac{\alpha_p}{\kappa_T} - p \tag{4}$$

Likewise, P_i, is related with internal energy, U, through eq 5):

$$P_i = \left(\frac{\partial U}{\partial V}\right)_T \tag{5}$$

Therefore, P_i may be particularly insightful when examining NADES due to its direct correlation with liquid cohesive forces. It essentially represents the pressure that arises from these intermolecular interactions within the liquid, and thus, it may be considered for analyzing and quantifying the strength of these intermolecular forces. When a NADES undergoes isothermal expansion, work against these cohesive forces is done, which is reflected in the changes in internal energy, which is precisely what P_i captures. A higher P_i indicates stronger intermolecular forces within the NADES. This information can be crucial for understanding various NADES properties, including their solvation behavior, viscosity, and thermal stability.

The uncertainties associated with the derived properties (α_p, κ_T, and P_i) originate from the propagation of the primary experimental error in ρ through the analytical expressions used (eqs 2−4). For α_p and κ_T, which involve first-order partial derivatives of ρ with respect to temperature and pressure, respectively, their uncertainties were estimated via numerical differentiation using polynomial fits of the $\rho(T,P)$ data (eq 1). The propagated error was assessed using standard error propagation theory and yields typical uncertainties of ±0.001 × 10^{-3} K^{-1} for α_p and ±0.1 TPa^{-1} for κ_T. These values correspond to relative uncertainties below 2% across the studied range, consistent with published work on similar vibrating-tube densimeter setups.[40] The internal pressure, P_i, is calculated using eq 4), which combines α_p, κ_T, as well as temperature and pressure, thereby compounding their uncertainties. Assuming uncorrelated errors and applying standard propagation, the uncertainty in P_i is estimated as ±0.1 MPa, which remains within 2−3% of typical values reported.[41]

2.2. PC-SAFT EoS Modeling. Pure component parameters are reported in Table 3.[42−44] These parameters were calculated from fits to the experimental saturated liquid density and vapor pressure, showing their reliability for the description of pure compound phase equilibria properties. The considered NADES were treated as binary mixtures of the corresponding components. THY was modeled as a 2B associative compound (i.e., hydrogen bond donor−acceptor), whereas CIN and CAMP were considered as nonassociative (i.e., only hydrogen bond acceptors). Mixtures (NADES) were treated considering a temperature independent binary interaction parameter k_{12} = −0.10 (THY:CIN) and k_{12} = −0.09 (THY:CAMP).

Table 3. Pure Component PC-SAFT Parameters for the NADES Components Considered in This Work as Obtained from the Literature[39−41]

compound	m_i^{seg}	σ_i /Å	ε_i/k_B(K)	N_{site}	ε^{AiBi}/k_B(K)	κ^{AiBi}/Å^3
THY	2.90	4.20	250.5	2B	3504.5	0.05
CIN	3.03	4.25	313.7			
CAMP	3.74	3.89	301.7			

2.3. Molecular Dynamics Simulations. *2.3.1. Modeling of Thymol-Based NADES Systems.* Systems were constructed using the Packmol software.[45] The molecular structures of the three components, highlighting their key functional groups, are illustrated in Figure 1a. The systems consisted of THY−CIN and THY−CAMP at experimental molar ratios of 1:1 and each cubic simulation box contained 500 molecules of thymol, and 500 molecules of cineole or camphor (Figure 3). The molecular structures of the NADES components were retrieved from the CHARMM Small Molecule Library through the CHARMM-GUI platform.

NADES composition	THY-CAMP	THY:CIN
Molar ratio	1:1	1:1
Number of molecule	500:500	500:500
Total number of atom	26000	27000
Configuration of the studied Systems		

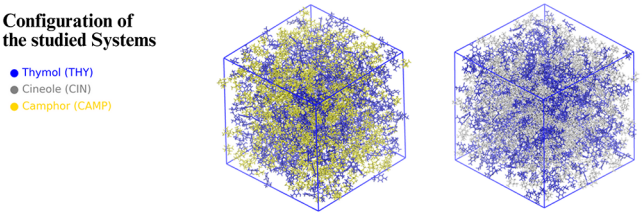

Figure 3. Structural and functional characteristics of thymol-based NADES systems.

Simulation details: Molecular dynamics (MD) simulations were initiated by minimizing the solvent energy for 10,000 steps (time step of 1 fs). Following minimization, the solvent system was equilibrated for 1 ns at 343.15 K and constant pressure (0.1 MPa). To facilitate mixing of the NADES components, a simulated annealing scheme similar to that of ref 46 was implemented, linearly increasing the temperature to 500 K over 100 ns and maintaining it at 500 K for 200 ns. Subsequently, the system was sequentially cooled down[47] to

https://doi.org/10.1021/acs.iecr.5c00116
Ind. Eng. Chem. Res. 2025, 64, 17958−17974

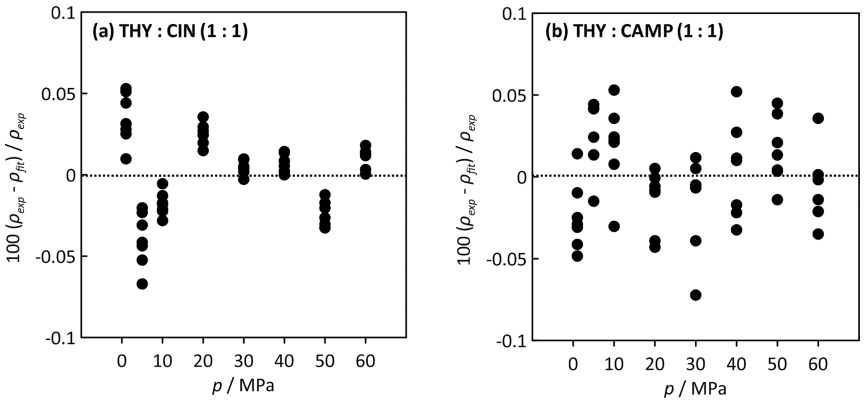

Figure 4. Results for (a) THY:CIN (1:1) and (b) THY:CAMP (1:1) NADES reporting the deviation between experimental density, ρ_{exp}, and density from fitting experimental $P\rho T$ data to eq 1), ρ_{fit}, with coefficients in Table 2.

experimental temperatures of 343.15, 323.15, 313.15, 303.15, and 293.15 K over 100 ns. The cooling process followed an exponential function as described in the following formula (t in ns)

$$T = 156.85e^{-0.05t} + 343.15 \quad (6)$$

initially achieving rapid cooling to 400 K within 20 ns, followed by slower cooling until the end of the simulation. Throughout these processes, pressure was maintained constant at 0.1 MPa. After each cooling step, the configuration obtained from the previous simulations was further evolved for 100 ns at specific temperatures: 343.15, 323.15, 313.15, 303.15, and 293.15 K, all maintained at a pressure of 0.1 MPa. Furthermore, the system at 303.15 K underwent additional simulations under varying pressures of 1, 5, 10, and 60 MPa, each for 100 ns. Similarly, simulations were conducted at 293.15, 313.15, 323.15, and 343.15 K under pressures of 10 and 60 MPa, respectively, also for 100 ns durations. Even at the lowest temperature at all pressures, the simulations were checked to be long enough for the molecules to diffuse on average at least 4 nm and to reorient completely and therefore sufficient to sample interactions and distributions. Formation of aggregates, if any, would take place on longer time scales.

All MD simulations were conducted using the GROMACS v.2022 software package.[48] The system was parametrized with the Charmm36[49] and CGenFF 4.6[50,51] force fields. The choice of the Charmm force field and the accompanying generalized CGenFF was motivated by its previous use for similar systems[52] and because it is well suited to describe general classes of molecules, including proteins, which may be important for other studies involving enzymes in the same solvents. A Verlet integrator and LINCS[53] constraints were used with a time step of 1 fs. Temperature was controlled via a modified Berendsen thermostat,[54] and an isotropic pressure of 0.1 MPa was maintained using a Parrinello−Rahman barostat[55] with a time constant of 2 ps and an isothermal compressibility of $4.5{\cdot}10^{-4}$ MPa^{-1}. The latter value, which refers to water at 1 bar and at 300 K, represents an educated guess before the experimental values were available. Long-range electrostatic interactions were described using the smooth Particle−Mesh Ewald (PME) method with a PME order of 4. Lennard−Jones and electrostatic interactions were calculated with a cutoff radius of 1.2 nm. The structural analysis of the MD trajectories was performed using the VMD software package,[56] GROMACS[48] and TRAVIS.[57]

3. RESULTS AND DISCUSSION

3.1. Experimental High-Pressure Behavior. The Experimental PVT (293.15 to 353.15 K and 1 to 60 MPa range) data for the investigated NADES (Table 1) were fitted to a 10-parameter model (eq 1), with the resulting fitting coefficients (Table 2) yielding excellent agreement with experimental data in the whole wide considered pressure−temperature range (Figure 4; deviations lower than 0.05%). These coefficients allowed for the accurate calculation of derived relevant thermodynamic properties (α_p, κ_T, and P_i) from experimental PVT data. NADES containing CAMP are slightly more dense than those with CIN in the whole studied range (+1.6% on average); nevertheless, they exhibited hydrophobic behavior with the consequence of lower density compared to water (0.91 to 0.99 g cm^{-3} for CIN systems and 0.93 to 1.00 g cm^{-3} for CAMP systems). Moreover, density (Figure 4a1,a2) displayed a linear relationship with increasing temperature and pressure ($R^2 > 0.999$ for the linear fits in all the cases).

The obtained α_p values (Figure 4b1,b2) were found to be within the range of $0.68-0.87 \times 10^{-3}$ K^{-1} for THY:CIN and 0.56 to 0.68×10^{-3} K^{-1} for THY:CAMP, indicating that systems with CAMP are remarkably less compressible (−17.8%) than those with CIN. Nevertheless, these α_p values are consistent with other hydrophobic type V NADES[30,34] but significantly higher than the values reported for (ionic) type III NADES.[31,32] The absence of ionic species in hydrophobic type V NADES leads to weaker intermolecular interactions, resulting in more compressible fluids compared to type III (ionic) (NA)DES. The temperature and pressure dependence of α_p was notably nonlinear (Figure 4b1,b2). Under isobaric conditions, α_p initially increased with temperature but then decreased, with the inflection point shifting to lower temperatures at higher pressures. This anomalous behavior has not been observed in other hydrophobic type V NADES[28] or type III NADES.[26] However, similar trends have been reported in some type III NADES,[26] type V NADES,[28] and ionic liquids.[58] This behavior of α_p is a thermodynamic anomaly and according to the requirements of α_p for the critical point of any fluid,[59] it must lead to minima in α_p vs temperature curves. These minima have not been found in the considered NADESs as the experimental measurements were carried out far from the critical point. The κ_T also exhibited a nonlinear behavior (Figure 4c1,c2), increasing with temperature and decreasing with pressure. κ_T values for the NADESs

https://doi.org/10.1021/acs.iecr.5c00116
Ind. Eng. Chem. Res. 2025, 64, 17958−17974

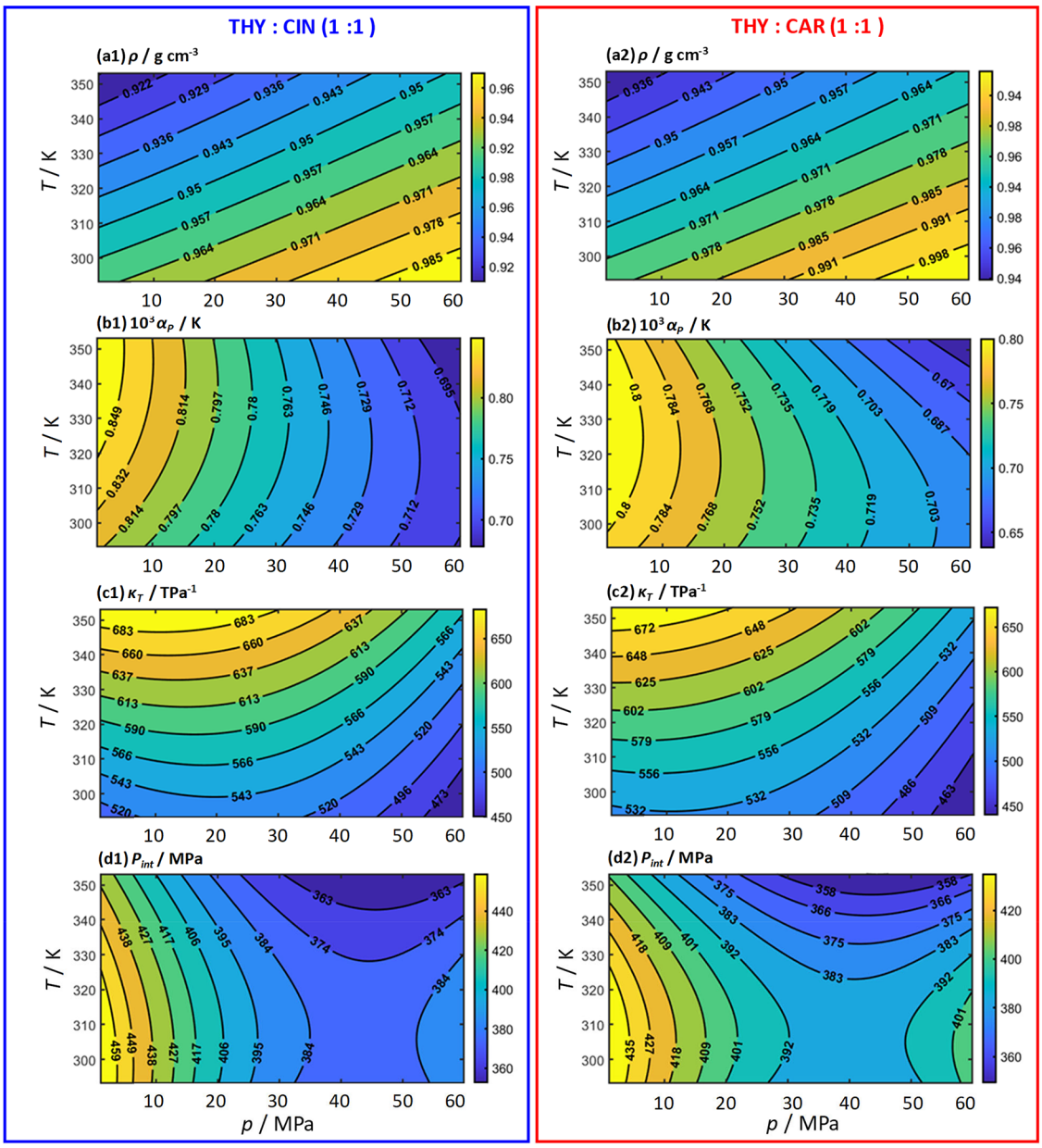

Figure 5. Results for THY:CIN (1:1) and THY:CAMP (1:1) NADES reporting experimental properties as a function of pressure and temperature plotting fit to eq 1) with coefficients in Table 2 for density and the corresponding calculated properties. (a1,a2) Density, ρ, (b1,b2) thermal expansion coefficient, α_P, (c1,c2) isothermal compressibility, κ_T, and (d1,d2) internal pressure, P_i.

were higher than those reported for type III NADES,[51−53] consistent with other type V NADES.[39]

The P_i displayed a complex behavior (Figure 4d1,d2), indicating the intricate nature of intermolecular forces in the considered NADES. The maxima observed in the P_i vs temperature plot suggest a change in fluid structure and intermolecular interactions at temperatures below 303 K. This behavior is characteristic of largely hydrogen-bonded fluids,[60] indicating the weakening of hydrogen bonds at higher temperatures. The minima observed in the P_i vs pressure plot are likely due to the increasing dominance of repulsive forces at high pressures, leading to a decrease in P_i. However, at very high pressures, the rearrangement of fluid structure can improve intermolecular interactions, resulting in a slope inversion. The cohesive energy density (ced), calculated from vaporization enthalpy and density, was found to be similar to P_i, suggesting a predominantly hydrogen-bonded nature of the NADES at all the considered pressure−temperature conditions.

As a result, the three calculated properties reflect the nature of the developed intermolecular forces. The α_p and κ_T coefficients reflect the responsiveness of the systems to thermal and mechanical perturbations, respectively. Their nonmonotonic behavior in these NADES is indicative of structural reorganizations, particularly involving hydrogen bonding networks. The presence of a maximum in α_p vs T implies a point where the effect of thermal agitation surpasses the ability of the hydrogen bonding network to accommodate volume changes without structural disruption. The P_i is linked to cohesive energy density and provides insight into the net balance between attractive and repulsive intermolecular interactions. The observed decrease in P_i with increasing

https://doi.org/10.1021/acs.iecr.5c00116
Ind. Eng. Chem. Res. 2025, 64, 17958−17974

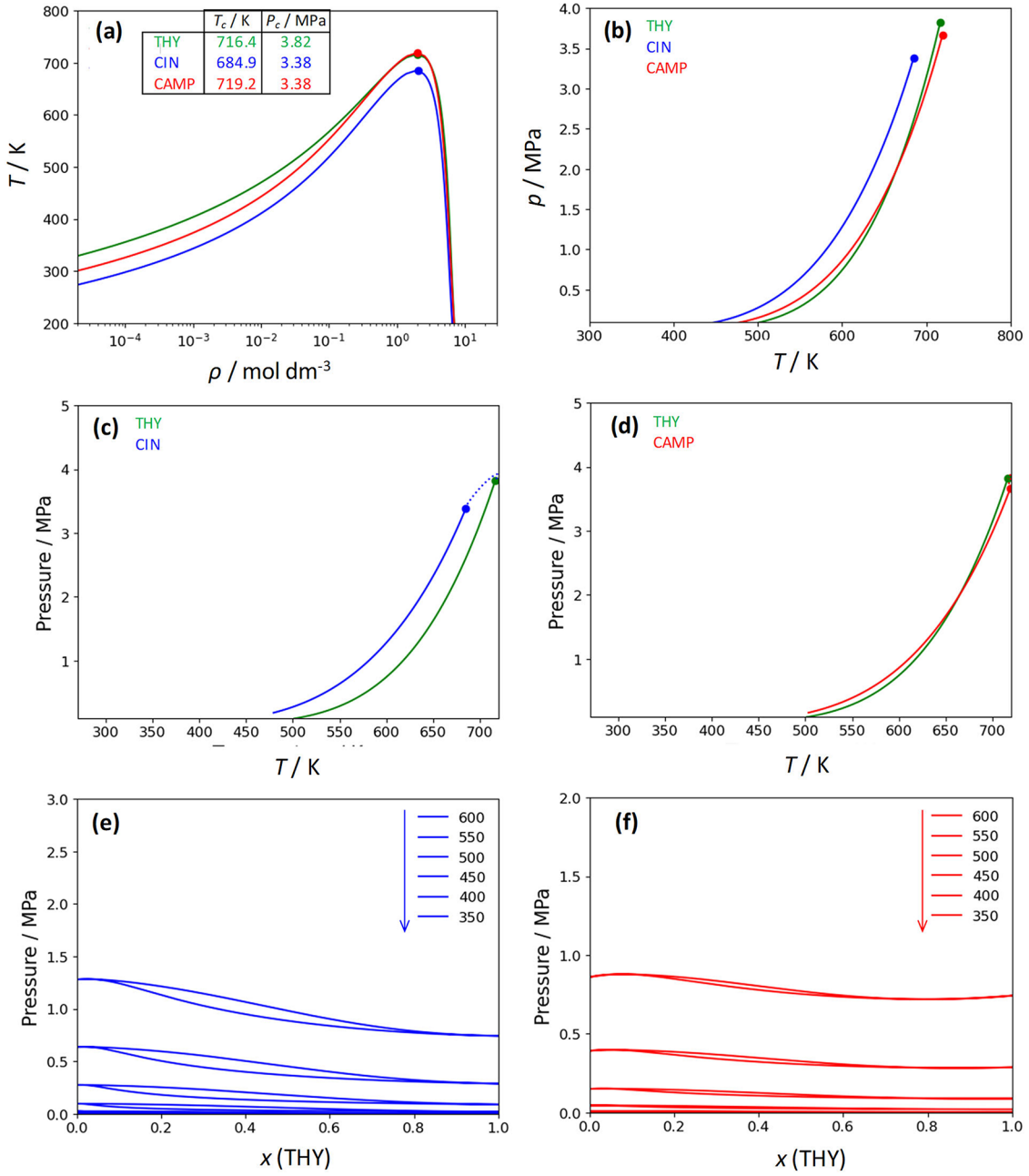

Figure 6. PC-SAFT predictions, pure compound parameters in Table 3, for (a) vapor−liquid saturation curves and (b) vapor pressures curves for pure compounds, with circles indicating predicted critical points, (c,d) global phase diagrams (type I according to the van Konynenburg classification) for THY:CIN and THY:CAMP (1:1) NADES, with dashed lines indicating critical locus, (e,f) isothermal vapor−liquid equilibria at the reported temperatures (in K). All the results for THY:CIN and THY:CAMP (1:1) NADES obtained with binary interaction parameter k_{12} = −0.10.

pressure, followed by a slope inversion at high pressure, likely results from two competing effects: (*i*) the compression-induced short-range repulsion, which initially suppresses P_i, and (*ii*) a restructuring of the hydrogen bond network at higher pressure, leading to an increase in cohesive forces and thus internal pressure. Therefore, the non-monotonic behavior of P_i vs pressure does not simply reflect a classical van der Waals-like interplay, but a pressure-induced reorganization of the liquid microstructure. This is especially prominent in the THY:CAMP system, where strong and frequent hydrogen bonds reorganize under compression, reinforcing cohesive forces despite increased density (Figure 5).

3.2. PC-SAFT Modeling. PC-SAFT modeling was employed to predict the properties of the NADES and its components. The saturation curve (Figure 6a) indicated that CIN and CAMP were slightly less dense than THY due to hydrogen bonding in neat THY. Both components exhibited high critical temperatures (CIN < THY < CAMP), resulting in negligible vapor pressures at close to ambient conditions (Figure 6b) and a Type I phase behavior (Figure 5c,d) at ambient conditions. The predicted isothermal vapor−liquid equilibria (Figure 5e,f) showed nonazeotropic behavior and low volatility. The solid−liquid equilibria (Figure 7) predicted a eutectic point at a THY:CIN mole ratio of 1:2 whereas for THY:CAMP the eutectic mixture is formed for equimolar

https://doi.org/10.1021/acs.iecr.5c00116
Ind. Eng. Chem. Res. 2025, 64, 17958−17974

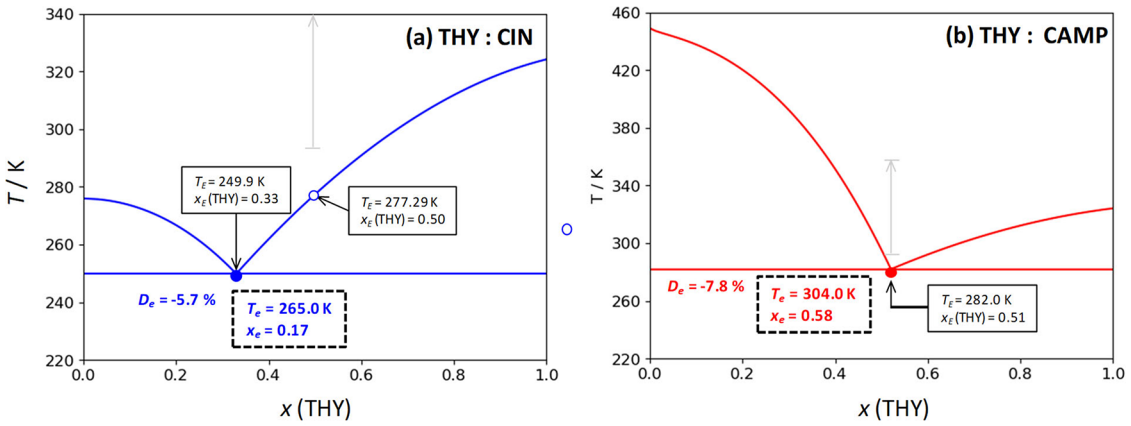

Figure 7. Solid−liquid equilibria, (a) for THY:CIN, (b) for THY:CAMP, predicted from PC-SAFT with parameters in Table 3 for THY:CIN and THY:CAMP (1:1) NADES obtained with binary interaction parameter k_{12} = −0.10. (Filled circles) eutectic point, (empty circles) equimolar composition considered in this work for experimental and computational studies, (gray arrows) temperature range considered in this work. Data in dashed squares show the composition and temperature for the eutectic point as inferred from ideal conditions, the D_e parameter for the differences among ideal and PC-SAFT predictions for the eutectic point is also reported.

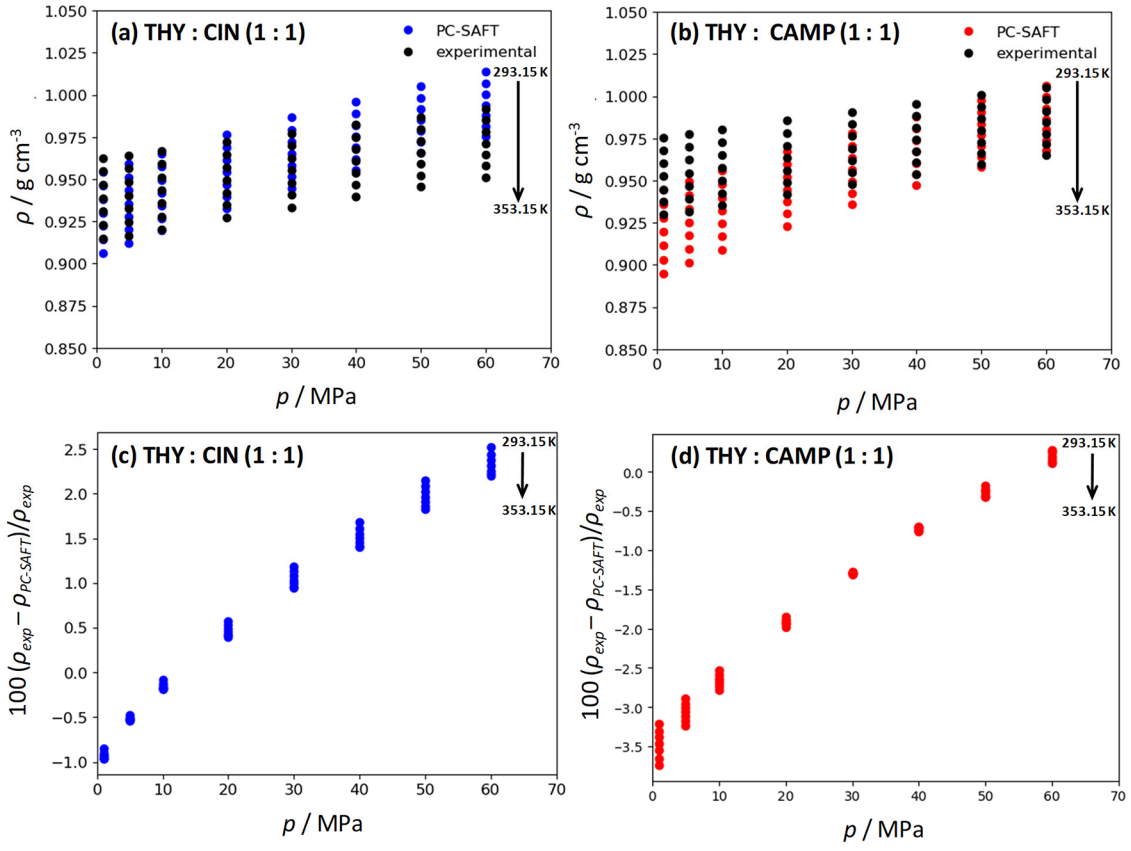

Figure 8. (a, b) PC-SAFT predictions for density (ρ) with pure compound parameters as reported in Table 3 and k_{12} = −0.10 for THY:CIN and THY:CAMP (1:1) NADES, (c, d) percentage deviations between experimental (exp) and predicted (PC-SAFT) density.

composition. In both cases, low melting temperatures are exhibited both for the eutectic point and equimolar mixtures, leading to liquid systems close to ambient conditions and making them suitable for industrial applications. Likewise, the D_e parameter, which quantified the depletion of eutectic temperature in comparison with ideal conditions,[61] was also calculated.

The predictive ability of PC-SAFT for the Solid−Liquid equilibria of the considered NADES is analyzed via comparison with experimental data. For the case of THY:CAMP (1:1) NADES the experimental Solid−Liquid diagram[27] shows the properties for the eutectic point being x_E (THY) = 0.54 and T_E = 230 K. The PC-SAFT predicted values in this work indicate a similar composition for the eutectic point (x_E (THY) = 0.51) whereas the T_E = 282 K is larger than the experimental value. Nevertheless, the ideal solid liquid equilibria is calculated showing an ideal T_E = 304.0 K, which K is larger than the PC-SAFT value, thus showing that the model is able to predict the nonideality of the considered NADES. The calculated D_e value among ideal behavior and PC-SAFT predictions is −7.8%, thus

https://doi.org/10.1021/acs.iecr.5c00116
Ind. Eng. Chem. Res. 2025, 64, 17958−17974

confirming nonideality and prediction of formation of a Deep Eutectic from PC-SAFT. Moreover, the considered THY:-CAMP 1:1 composition considered in this work for High Pressure studies correspond to the true eutectic point. Likewise, these large deviations from ideality are a consequence of the extension and complexity of developed hydrogen bonding, the PC-SAFT modeling uses a single (nontemperature/noncomposition dependent) binary interaction parameter which averages the complex intermolecular interactions landscape.

For the case of THY:CIN (1:1), experimental solid−liquid equilibria data is absent from the literature, and thus, no comparison is possible. Nevertheless, the PC-SAFT calculated Solid−Liquid equilibria, Figure 7, show the formation of a eutectic point for THY:CIN 1:2 mole fraction. The Solid−Liquid equilibria for ideal behavior show a higher temperature in comparison with PC-SAFT predictions with a $D_e = -5.7\%$, i.e. confirming the formation of a Deep Eutectics, and thus showing that PC-SAFT model is able to predict systems nonideality. It should be remarked that the considered composition for THY:CIN High pressure study (1:1) does not correspond to the true eutectic point, which would be around 1:2. Therefore, although the term Deep Eutectic in the thermodynamic sense refers to a specific point in the Solid−Liquid Equilibria of the mixture yet the term DESs is broadly used in the literature to refer to more than just that thermodynamic eutectic point, as in the case of THY:CIN. Nevertheless, the recently proposed Low Melting Mixtures (LMMs)[62,63] term defining those mixtures which although not being exactly the corresponding eutectic point are liquid at atmospheric pressure and show melting temperatures below those under ideal conditions could be used for the system THY:CIN 1:1. The selection of 1:1 composition was done in parallel to that for THY:CAMP, for which 1:1 composition is the true eutectic point, with the objective of comparing both systems at the same mole ration in spite of THY:CIN 1:1 being truly a LMM. Therefore, the nomenclature DES is also maintained for THY:CIN (1:1) with the caveat that the true eutectic point is predicted at (1:2) composition.

Likewise, PVT data were predicted using PC-SAFT with a single temperature/pressure-independent binary interaction parameter (BIP). The negative sign of the BIP (−0.10) indicated hydrogen bonding between THY and CIN/CAMP, and, considering the complex intermolecular forces landscape leading to the properties patterns (Figure 5) to be described with the simplicity of a constant BIP, PC-SAFT led to suitable PVT predictions, Figure 8. Nevertheless, PC-SAFT slightly underpredicted density at low pressures for THY:CIN (Figure 8a), with deviations around 2%, whereas for THY:CAMP an overprediction is inferred for low pressure conditions with worse predictions upon compression (Figure 8b). The use of temperature/pressure-dependent BIPs and the inclusion of polar terms in the EoS (PCP-SAFT) could potentially improve the accuracy of PC-SAFT predictions, especially at high pressures and temperatures.

3.3. Nanostructuring under Compression from MD Simulations. The density results from the MD simulations were initially compared with experimental values (Table 4). While the calculated densities are, on average, 3% smaller than experimental data, they exhibit strong correlation (0.87) across varying pressures and temperatures. Both experimental and theoretical densities tend to decrease with higher temperatures. Conversely, and as expected, increasing the pressure from 0.1 to 60 MPa increases the mixture's density. The MD simulation results depend on the accuracy of the force field and reproduce well the trends of the experimental data with temperature and pressure, although the absolute agreement with data is limited. It should also be noted that the experimental dependence of density on pressure is found, in general, to be larger than that obtained by MD simulation. However, increasing the temperature tends to reduce these discrepancies.

Table 4. Experimental (EXP) and Computational (MD) Densities (ρ) for THY:CIN (1:1) DES and THY:CAMP (1:1) DES

		THY:CIN (1:1)		THY:CAM (1:1)	
T/K	$P/$ MPa	ρ_{EXP}/g cm^{-3}	ρ_{MD}/g cm^{-3}	ρ_{EXP}/g cm^{-3}	ρ_{MD}/g cm^{-3}
293.15	0.1	0.9620	0.9269	0.9730	0.9491
	10	0.9668	0.9275	0.9792	0.9502
	60	0.9917	0.9304	1.0026	0.9543
303.15	0.1	0.9543	0.9253	0.9662	0.9483
303.15	1	0.9547	0.9256	0.9669	0.9476
	5	0.9563	0.9257	0.9699	0.9482
	10	0.9590	0.9259	0.9729	0.9489
	60	0.9850	0.9290	0.9968	0.9529
313.15	0.1	0.9463	0.9238	0.9601	0.9444
	10	0.9512	0.9247	0.9663	0.9478
	60	0.9782	0.9280	0.9911	0.9520
323.15	0.1	0.9382	0.9213	0.9536	0.9389
	10	0.9434	0.9233	0.9598	0.9438
	60	0.9713	0.9271	0.9859	0.9510
343.15	0.1	0.9224	0.9062	0.9409	0.9218
	10	0.9279	0.9124	0.9465	0.9289
	60	0.9579	0.9252	0.9742	0.9492

The radial distribution functions, $g(r)$ for the THY:CIN/CAMP trajectories were also analyzed. The analyses were focused on oxygen atoms, because the frequency of contacts involving the oxygen of thymol were at all temperatures and pressures ca. two times larger than expected based on a random distribution of contacts, highlighting the importance of hydrogen bonding in the mixtures, with a sizable preference for cineole or camphor, over other thymol molecules. The analysis of much less pronounced preferences of carbon−carbon contacts was uncertain, also because of the indirect correlations induced by hydrogen bonding interactions.

The positions of the peaks are related to the strength of the interactions, whereas their heights are related to the frequency of that distance. The width of the peaks gives information about the restraints on the interactions. Thus, the narrower the peak, the more constrained is the interaction. The analysis focused on two specific hydrogen bond interactions: those between the hydroxyl group (O1−H5) of Thymol, where Thymol acts as hydrogen bond donor, and the oxygen atom (O1) of Cineole, as hydrogen bond acceptor (see Figure 9a). Also, the interactions between pairs of Thymol molecules were examined, with Thymol acting as the hydrogen bond donor and acceptor (see Figure 9b).

Figure 9c depicts the $g(r)$ graph that varies with increasing pressure at a constant temperature of 303.15 K. For the THY(OH)−CIN(O) systems, the distance values for the highest radial distribution function (RDF) peaks were 188.3, 188.3, 191.7, 185.0, and 191.7 pm at pressures of 0.1, 1, 5, 10, and 60 MPa, respectively. This nonmonotonous behavior leads to shallow maximum, which results from a complex (subtle)

https://doi.org/10.1021/acs.iecr.5c00116
Ind. Eng. Chem. Res. 2025, 64, 17958−17974

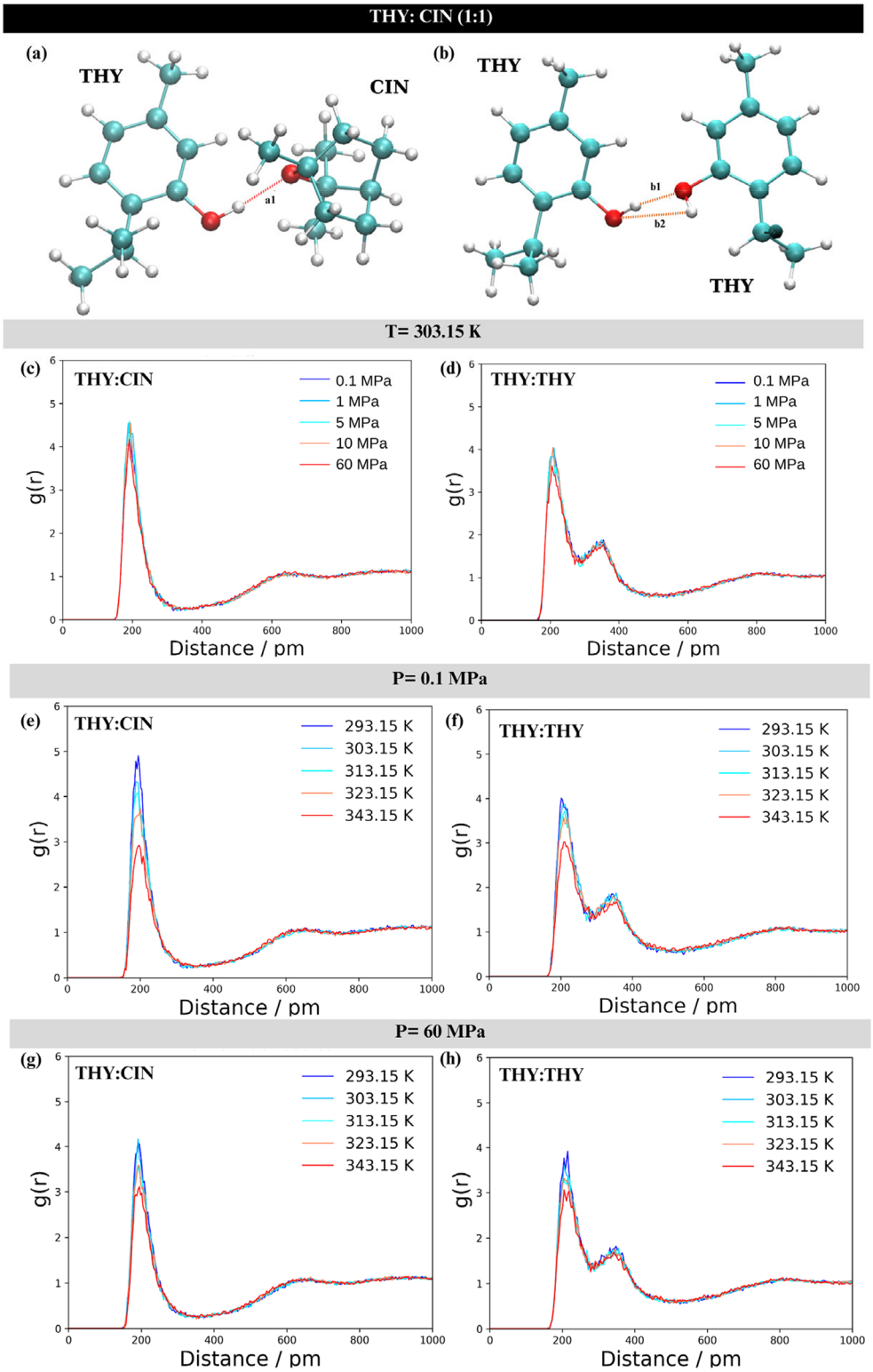

Figure 9. Structural representations of the THY:CIN 1:1 system. The interactions are as follows: (a) THY(OH)−CIN(O), with the hydrogen bond distance labeled as a1, and (b) THY(OH)−THY(OH), with the potential bond distances labeled as b1 and b2. Radial distribution functions, $g(r)$, are described for the THY(OH)−CIN(O) under the following conditions: (c) at 303.15 K and 0.1 to 60 MPa, (e) at 0.1 MPa from 293.15 to 343.15 K, and (g) at 60 MPa from 293.15 to 343.15 K. RDFs for THY(OH)−THY(OH) are presented at: (d) 303.15 K and 0.1 to 60 MPa, (f) 0.1 MPa from 293.15 to 343.15 K, and (h) 60 MPa from 293.15 to 343.15 K. The first (intense and narrow) peaks in the reported radial distribution functions correspond to the formation of hydrogen bonding for the corresponding pairs.

structural evolution under pressure. The corresponding $g(r)$ values were 4.3, 4.5, 4.6, 4.1, and 4.2, respectively, showing a shallow maximum about 5 MPa. The primary interaction distance is therefore not significantly influenced by pressure changes. Also, higher pressures lead to greater structural organization and stronger interactions within the system.

https://doi.org/10.1021/acs.iecr.5c00116
Ind. Eng. Chem. Res. 2025, 64, 17958−17974

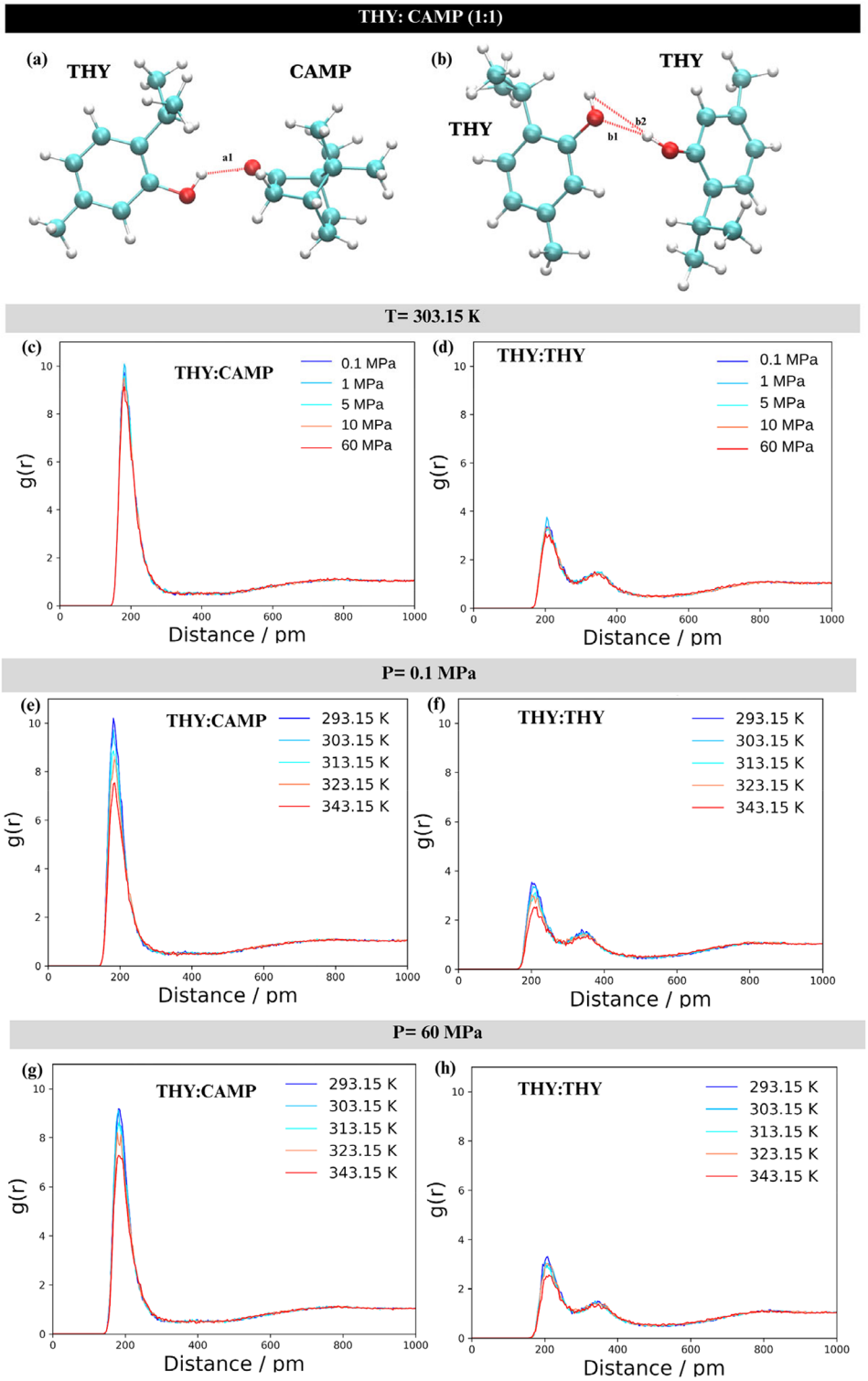

Figure 10. Structural representations of the THY:CAMP 1:1 system. The interactions are as follows: (a) THY(OH)−CAMP(O), with the hydrogen bond distance labeled as a1, and (b) THY(OH)−THY(OH), with the potential bond distances labeled as b1 and b2. Radial distribution functions, $g(r)$, are described for the THY(OH)−CIN(O) under the following conditions: (c) at 303.15 K and 0.1 to 60 MPa, (e) at 0.1 MPa from 293.15 to 343.15 K, and (g) at 60 MPa from 293.15 to 343.15 K. RDFs for THY(OH)−THY(OH) are presented at: (d) 303.15 K and 0.1 to 60 MPa, (f) 0.1 MPa from 293.15 to 343.15 K, and (h) 60 MPa from 293.15 to 343.15 K. The first (intense and narrow) peaks in the reported radial distribution functions correspond to the formation of hydrogen bonding for the corresponding pairs.

Beyond the primary peak, the $g(r)$ curves exhibit a gradual decline toward a value of 1, which aligns with a homogeneous distribution. Figure 9d shows the $g(r)$ curves associated with the THY(OH):THY(OH) H-bond interaction at different pressure values and at 303.15 K. Their profile exhibits in this case two pronounced peaks, indicating the presence of two distinct interaction distances between Thymol molecules within the system. The distance values for the first highest

https://doi.org/10.1021/acs.iecr.5c00116
Ind. Eng. Chem. Res. 2025, 64, 17958−17974

peak were 211.7, 208.3, 208.3, 208.3, and 205.0 pm at pressures of 0.1, 1, 5, 10, and 60 MPa, respectively. Their corresponding $g(r)$ values were 3.9, 4.0, 3.9, 4.0, and 3.6, respectively, almost unaffected by changes in pressure up to 10 MPa. The first peak corresponds to the strong interaction between two Thymol molecules in the closest hydrogen bonding arrangement, shown as distance b1 in Figure 9b. The second broader peak is associated with the slightly longer distance between Thymol oxygen and hydrogen not involved directly in the hydrogen bond, denoted distance b2 in Figure 9b. The $g(r)$ in Figure 8e,f were obtained at a constant pressure of 0.1 MPa across a range of temperatures from 293.15 to 343.15 K, to assess the influence of temperature on the intermolecular interactions at the low-pressure regime of the system. Figure 9e shows the RDF curves for the THY-(OH):CIN(O) H-bond interaction at different temperatures and 0.1 MPa. The distance values were 188.3, 188.3, 195.0, 191.7, and 198.3 pm at 293.15, 303.15, 313.15, 323.15, and 343.15 K, respectively. The corresponding $g(r)$ values were 4.8, 4.3, 4.1, 3.6, and 2.9, respectively. The $g(r)$ peaks become less pronounced with increasing temperature, indicating reduced structural organization and weaker interactions within the system at higher temperatures. For THY(OH):THY(OH) H-bond interaction (Figure 9f) the distance values for the first highest peak were 201.7, 211.7, 211.7, 208.3, and 211.7 pm at same temperature range and the corresponding $g(r)$ values were 4.0, 3.9, 3.7, 3.6, and 3.0, respectively. The $g(r)$ peaks in Figure 9f show a smaller decrease with rising temperature compared to the THY(OH):CIN(O) system this indicating that THY(OH):THY(OH) interactions are less affected by temperature changes, most likely because of the double possibility to form H-bonds. The $g(r)$ shown in Figure 8g,h were obtained at the higher pressure of 60 MPa, covering the same temperature range as before. The distance values for Figure 9g were 191.7, 191.7, 191.7, 191.7, and 185.0 pm respectively, while the corresponding $g(r)$ values were 4.1, 4.2, 3.6, 3.6, and 2.9, respectively. The $g(r)$ trends observed in Figure 9g at the higher pressure of 60 MPa closely resemble those seen at 0.1 MPa, where elevated temperatures lead to a reduction in peak heights, though the changes are less pronounced at the higher pressure. The distance values for Figure 9h were 215.0, 205.0, 215.0, 205.0, and 205.0 pm, respectively, while the corresponding $g(r)$ values were 3.9, 3.6, 3.3, 3.3, and 3.1, respectively. As illustrated in Figure 9h, similar temperature-dependent trends were observed at the high pressure of 60 MPa, although the changes were less pronounced compared to the low-pressure scenario. This indicates that pressure significantly affects the structural integrity and interaction strength within the CIN−THY system.

The CAMP and CIN systems under varying pressures at 303.15 K reveal notable differences. In the CAMP system, the $g(r)$ values for THY(OH):CAMP(O) interactions are significantly higher (see Figure 10c), indicating more frequent hydrogen bonds and a more organized structure compared to the CIN system, as apparent from the directionality in the spatial distribution maps (Figure 11). The $g(r)$ values for THY(OH):CAMP(O) interactions reach up to 10.1, whereas the highest $g(r)$ value for THY(OH):CIN(O) is 4.6. This suggests that CAMP forms more frequent hydrogen bonds with thymol than CIN does. Additionally, the $g(r)$ positions in the CAMP system are slightly shorter (181.7 pm) than in the CIN system (188.3 pm), indicating a closer interaction in the

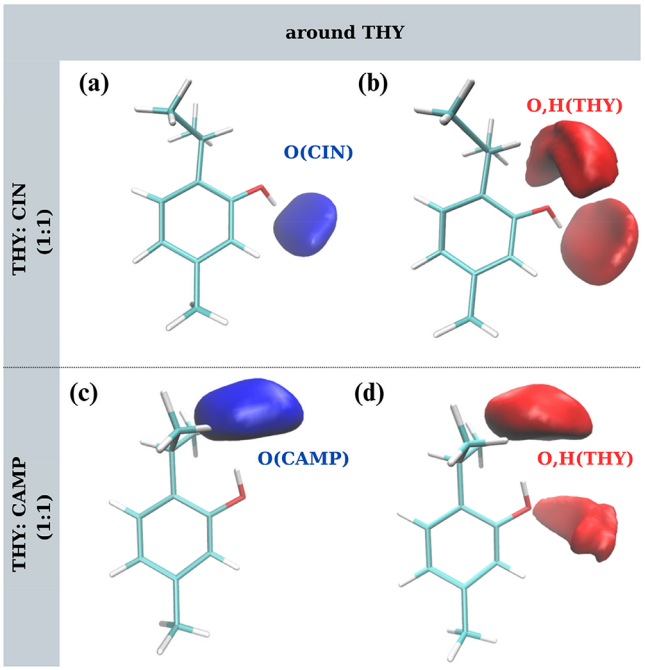

Figure 11. Spatial distribution function (SDF) analysis of thymol interacting with cineole (1:1) and camphor (1:1). For the THY:CAMP system, panel (a) displays the preferred location of cineole's oxygen atom (blue) around thymol, and panel (b) shows the position of thymol's oxygen and hydrogen atoms (red). For the THY:CAMP system, panel (c) displays preferred location of camphor's oxygen atom (blue) and panel (d) shows the positions of thymol's oxygen and hydrogen atoms (red).

former. For the THY(OH):THY(OH) interactions, both systems show similar trends with pressure. However, the peak heights in the CAMP system are lower (see Figure 10d), suggesting weaker THY−THYinteractions when CAMP is present compared to CIN. This reduction is likely due to thymol competing interaction with CAMP. When comparing temperature effects at 0.1 MPa, the THY(OH):CAMP(O) interactions in the CAMP system show higher $g(r)$ values (see Figure 10e) than those in the CIN system across all temperatures. The peak distances for THY(OH):CAMP(O) interactions appear at 181.7 pm at lower temperatures, with a slight increase to 185.0 pm at higher temperatures (323.15 and 343.15 K). The $g(r)$ values decrease from 10.7 at 293.15 K to 7.5 at 343.15 K. This indicates that the CAMP system maintains frequent hydrogen bonding even as temperature increases, although both systems exhibit a decrease in $g(r)$ values with rising temperature. For the THY(OH):THY(OH) interactions, both systems show a decrease in peak height with increasing temperature (see Figure 10f), but the CIN system has higher $g(r)$ values, indicating more frequent thymol−thymol interactions. This is consistent with the stronger competing interaction in the CAMP system. At 60 MPa, the trends observed at 0.1 MPa are generally preserved (see Figure 10g,h), but the differences between the CAMP and CIN systems are less pronounced. Both systems show reduced sensitivity to temperature changes under higher pressure, but the CAMP system continues to exhibit higher $g(r)$ values for THY(OH):CAMP(O) interactions, highlighting more frequent hydrogen bonding compared to the CIN system. A summary of the total number of hydrogen bonds per time frame at different temperatures and pressures is reported in

https://doi.org/10.1021/acs.iecr.5c00116
Ind. Eng. Chem. Res. 2025, 64, 17958−17974

Figure 12. The differences in hydrogen bonding highlight the influence of the specific molecular structure on the nature and strength of intermolecular interactions within NADES systems.

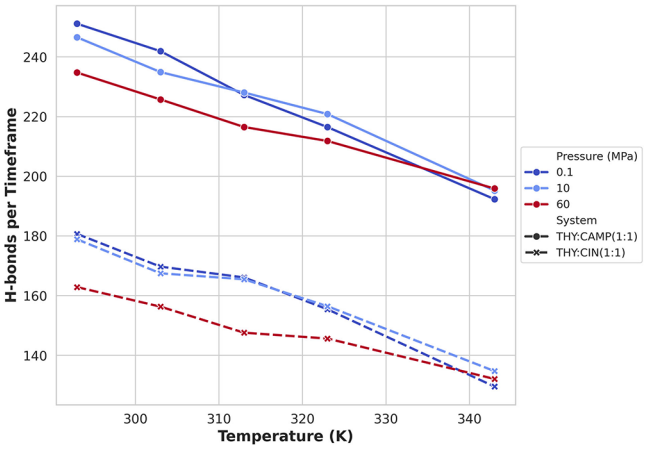

Figure 12. Number of hydrogen bonds per time frame as a function of temperature for THY:CIN (1:1) and THY:CAMP (1:1) systems at different pressures.

In order to validate the sufficiency of the 100 ns MD simulations for sampling molecular organization and interactions, we repeatedly chose two molecules (one for each molecular type) and visually checked that they diffuse, reorient and interact with different molecules along the trajectory. A superposition of two molecules along the trajectory for the simulations at 313 K and 10 MPa is reported in Figure 13.

3.4. Integration between Experimental and Modelized Results. The integration of experimental measurements and MD simulations provides a comprehensive picture of nanostructuring in the considered NADES under various conditions, considering the high-pressure effects. MD simulations yielded densities approximately 3% smaller than experimental values but showed a strong correlation (0.87) across varying pressures and temperatures. Both approaches demonstrated density decreases with higher temperatures and increases with higher pressures, validating the MD model for estimating NADES densities. While experimental density showed a stronger pressure dependence than MD simulations, temperature increases reduced these discrepancies. The differences observed in the densities between experiments and simulations are likely due to force field inaccuracies and difficult to avoid in general force fields without extensive reparametrization. Indeed, differences of similar absolute magnitude have been found even using the supposedly more accurate, polarizable force field Amoeba on similar systems.[64] Another possible explanation is the presence of microheterogenities that may affect the density, similar to the effects on experimental viscosities which are ca. 1 order of magnitude larger than the ones computed from the diffusion constants and molecular sizes from MD simulations.[63] No hint at such heterogeneities was found on the time scale of simulations, resulting in viscosities, under the simulated conditions, between 1 and 6 mPa s, indeed much smaller than the experimental ones.

This convergence at higher temperatures, i.e. where heterogeneity is less likely, suggests that MD can accurately represent system behavior. MD simulations complemented experimental findings by providing atomic-level insights revealing complex structural evolution under pressure for both NADES. Both experimental and MD results indicated that pressure enhances structural organization and strengthens interactions, while temperature weakens them. MD simulations further elucidated system-specific behaviors, showing more frequent hydrogen bonding and organized structure in THY−CAMP compared to THY−CIN. This aligns with experimental observations of system-dependent properties and highlights the influence of molecular structure on NADES behavior.

The combined approach reveals that while pressure generally enhances structural integrity, temperature weakens intermolecular interactions, with effects less pronounced at higher pressures. This interplay, observed in both experimental and MD results, underscores the complex nanostructuring behavior in NADES. By bridging macroscopic experimental measurements with microscopic MD insights, this study provides a nuanced understanding of how molecular interactions translate to bulk properties.

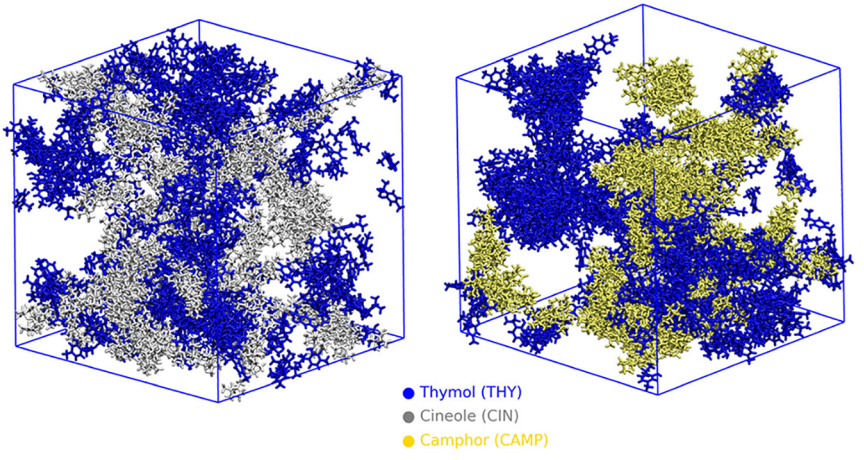

Figure 13. Superposition of snapshots of two molecules (one for each type) taken at 1 ns intervals along the 100 ns MD trajectory at 313 K and 10 MPa. The left panel illustrates the distribution of thymol (blue) and cineole (gray), while the right panel shows thymol (blue) and camphor (yellow), highlighting molecular translational and rotational diffusion.

https://doi.org/10.1021/acs.iecr.5c00116
Ind. Eng. Chem. Res. 2025, 64, 17958−17974

4. CONCLUSIONS

Two thymol based NADES, THY:CIN(1:1) and THY:CAMP(1:1), have been characterized experimentally and by molecular dynamics simulations, in the range of temperatures (293.15 to 343.15 K) and pressures (0.1 to 60 MPa). The densities are lower than water in all conditions and slightly larger for CAMP than for CIN, likely due to the slightly larger molecular volume of the latter.

Both in experiments and simulations the density decreases with increasing temperature and increases with pressure, as expected. In order to rationalize experimental data, we focused on hydrogen bonding, as described in Molecular Dynamics simulations. These show that the CAMP and CIN systems exhibit notable differences under varying pressures at 303.15 K. The CAMP system shows significantly more frequent hydrogen bonding and a more organized structure compared to the CIN system. Stronger interactions in the former compared to the latter are consistent with a more polar carboxyl versus ether oxygen. For THY−THY interactions, both systems display similar pressure-dependent trends, but we observe weaker interactions when camphor is present, due to the competing interactions with camphor molecules. Indeed, when comparing temperature effects at fixed pressures, we observe stronger THY−CAMP, with respect to THY−CIN, interactions across all temperatures, indicating more frequent hydrogen bonding. However, both systems show a decrease in the frequency of hydrogen bonding interactions with rising temperature, as expected. For THY(OH): THY(OH) interactions, the CIN system displays stronger interactions compared to the CAMP system, consistent with the weaker competition from cineole, compared to camphor. At high pressure, these trends persist, though both systems show reduced sensitivity to temperature changes. It is remarkable that both changes in hydrogen bonding and in internal pressure as derived from experiments are amounting to at most 25% upon changes in pressure of about 60 MPa. The differences in hydrogen bonding, with stronger hydrogen bonding (determining cohesive forces) and a more organized structure across varying pressures and temperatures for the CAMP system, confer outstanding different properties in internal pressure as derived by experiments. The balance of the two contributions with their different sensitivity to temperature and pressure may result in a complex dependence of cohesive forces and therefore in internal pressure. Indeed, the effect of pressure on internal pressure is not monotonic showing a maximum for CAMP systems, whereas a shallow minimum is present at all temperatures for the CIN systems. These findings underscore the impact of molecular structure on intermolecular interactions within NADES systems and show the richness of behavior that can be obtained.

AUTHOR INFORMATION

Corresponding Authors

Federico Fogolari − *Dipartamento di Scienze Matematiche, Informatiche e Fisiche, University of Udine, 33100 Udine, Italy;* orcid.org/0000-0001-9862-250X; Email: federico.fogolari@uniud.it

Santiago Aparicio − *Department of Chemistry and International Research Center in Critical Raw Materials for Advanced Industrial Technologies (ICCRAM), University of Burgos, 09001 Burgos, Spain;* orcid.org/0000-0001-9996-2426; Email: sapar@ubu.es

Authors

Ozge Ozkilinc − *Dipartamento di Scienze Matematiche, Informatiche e Fisiche, University of Udine, 33100 Udine, Italy; Department of Chemistry, University of Burgos, 09001 Burgos, Spain*

Alfredo Bol-Arreba − *Department of Physics and International Research Center in Critical Raw Materials for Advanced Industrial Technologies (ICCRAM), University of Burgos, 09001 Burgos, Spain;* orcid.org/0000-0003-4641-4826

Miguel Angel Soler − *Dipartamento di Scienze Matematiche, Informatiche e Fisiche, University of Udine, 33100 Udine, Italy;* orcid.org/0000-0002-5780-9949

Complete contact information is available at: https://pubs.acs.org/10.1021/acs.iecr.5c00116

Notes

The authors declare no competing financial interest.

ACKNOWLEDGMENTS

This work was funded by Agencia Estatal de Investigación (Spain, Project NADES for PFAS, ref.: PID2022-142405OB-I00) and Junta de Castilla y León (Spain, Project NADESforNature, ref.: BU047P23). We also acknowledge SCAYLE (Supercomputación Castilla y León, Spain) for providing supercomputing facilities. M.S. and O.O. are supported by the Italian Ministry of the University and the Research via the research program PON 2014-2020 AZIONE IV.6 GREEN, project numbers 2021RTDA46_02B2_DMIF and DOT215B2RJ, respectively. The statements made herein are solely the responsibility of the authors.

REFERENCES

(1) Clarke, C. J.; Tu, W.; Levers, O.; Bröhl, A.; Hallett, J. P. Green and Sustainable Solvents in Chemical Processes. *Chem. Rev.* **2018**, *118*, 747−800.

(2) United Nations. Transforming Our World: The 2030 Agenda for Sustainable Development; United Nations: New York, 2015. https://sdgs.un.org/2030agenda (accessed Sept 1, 2024).

(3) Abbott, A. P.; Capper, G.; Davies, D. L.; Rasheed, R. K.; Tambyrajah, V. Novel Solvent Properties of Choline Chloride/Urea Mixtures. *Chem. Commun.* **2003**, *9*, 70−71.

(4) Abbott, A. P.; Capper, G.; Gray, S. Design of Improved Deep Eutectic Solvents Using Hole Theory. *Chem.−Eur. J.* **2006**, *7*, 803−806.

(5) Wazeer, I.; Hayyan, M.; Hadj-Kali, M. K. Deep Eutectic Solvents: Designer Fluids for Chemical Processes. *J. Chem. Technol. Biotechnol.* **2018**, *93*, 945−958.

(6) Smith, E. L.; Abbott, A. P.; Ryder, K. S. Deep Eutectic Solvents (DESs) and Their Applications. *Chem. Rev.* **2014**, *114*, 11060−11082.

(7) Abranches, D. O.; Martins, M. A. R.; Silva, L. P.; Schaeffer, N.; Pinho, S. P.; Coutinho, J. A. P. Phenolic Hydrogen Bond Donors in the Formation of Non-Ionic Deep Eutectic Solvents: The Quest for Type V DES. *Chem. Commun.* **2019**, *55*, 10253−10256.

(8) Fan, C.; Sebbah, T.; Liu, Y.; Cao, X. Terpenoid-Capric Acid Based Natural Deep Eutectic Solvent: Insight into the Nature of Low Viscosity. *Clean Eng. Technol.* **2021**, *3*, No. 100116.

(9) Zamora, L.; Benito, C.; Gutiérrez, A.; Alcalde, R.; Alomari, N.; Al Bodour, A.; Atilhan, M.; Aparicio, S. Nanostructuring and Macroscopic Behavior of Type V Deep Eutectic Solvents Based on Monoterpenoids. *Phys. Chem. Chem. Phys.* **2022**, *24*, 512−531.

(10) Cao, J.; Su, E. Hydrophobic Deep Eutectic Solvents: The New Generation of Green Solvents for Diversified and Colorful Applications in Green Chemistry. *J. Clean. Prod.* **2021**, *314*, No. 127965.

(11) Dai, Y.; van Spronsen, J.; Witkamp, G. J.; Verpoorte, R.; Choi, Y. H. Natural Deep Eutectic Solvents as New Potential Media for Green Technology. *Anal. Chim. Acta* **2013**, *766*, 61−68.
(12) Florindo, C.; Branco, C.; Marrucho, M. I. Quest for Green-Solvent Design: From Hydrophilic to Hydrophobic (Deep) Eutectic Solvents. *Chem.−Eur. J.* **2019**, *12*, 1549−1559.
(13) Radošević, K.; Curko, N.; Srček, V. G.; Bubalo, M. C.; Tomasevic, M.; Gonić, K. K.; Redovnikovic, I. R. Natural Deep Eutectic Solvents as Beneficial Extractants for Enhancement of Plant Extracts Bioactivity. *LWT* **2016**, *73*, 45−51.
(14) Kalhor, P.; Ghandi, K. Deep Eutectic Solvents for Pretreatment, Extraction, and Catalysis of Biomass and Food Waste. *Molecules* **2019**, *24*, 4012.
(15) van Osch, D. J.; Zubeir, L. F.; van den Bruinhorst, A.; Rocha, M. A.; Kroon, M. C. Hydrophobic Deep Eutectic Solvents as Water-Immiscible Extractants. *Green Chem.* **2015**, *17*, 4518−4521.
(16) Abdelquader, M. M.; Li, S.; Andrews, G. P.; Jones, D. S. Therapeutic Deep Eutectic Solvents: A Comprehensive Review of Their Thermodynamics, Microstructure and Drug Delivery Applications. *Eur. J. Pharm. Biopharm.* **2023**, *186*, 85−104.
(17) van Osch, D. J. D. P.; Dietz, C. H. J. T.; van Spronsen, J.; Gallucci, G.; van Sint, M.; Tuinier, R.; et al. ASearch for Natural Hydrophobic Deep Eutectic Solvents Based on Natural Components. *ACS Sustainable Chem. Eng.* **2019**, *7*, 2933−2942.
(18) García, G.; Aparicio, S.; Ullah, R.; Atilhan, M. Deep Eutectic Solvents: Physicochemical Properties and Gas Separation Applications. *Energy Fuels* **2015**, *29*, 2616−2644.
(19) Al-Bodour, N. A.; Alomari, N.; Gutiérrez, A.; Aparicio, S.; Atilhan, M. High-Pressure Carbon Dioxide Solubility in Terpene-Based Deep Eutectic Solvents. *J. Environ. Chem. Eng.* **2022**, *10*, No. 108237.
(20) Li, Y.; Fan, X.; Cai, M.; Xu, X.; Zhu, M.; et al. Green and Economical Bet-Based Natural Deep Eutectic Solvents: A Novel High-Performance Lubricant. *ACS Sustainable Chem. Eng.* **2022**, *10*, 7253−7264.
(21) Li, Y.; Li, H.; Fan, X.; Xu, X.; Zhu, M. Oil-Soluble Deep Eutectic Solvent as High-Performance Green Lubricant Additives for PAO 40 and PEG 200. *Tribol. Int.* **2023**, *186*, No. 108602.
(22) Padilla, N.; Delso, I.; Bergua, F.; Lafuente, C.; Artal, M. Characterization of Camphor: Thymol or dl-Menthol Eutectic Mixtures: Structure, Thermophysical Properties, and Lidocaine Solubility. *J. Mol. Liq.* **2024**, *405*, No. 125069.
(23) Rozas, S.; Benito, C.; Alcalde, R.; Atilhan, M.; Aparicio, S. Insights on the Water Effect on Deep Eutectic Solvents Properties and Structuring: The Archetypical Case of Choline Chloride + Ethylene Glycol. *J. Mol. Liq.* **2021**, *344*, No. 117717.
(24) Verevkin, S. P. Determination of the Ortho-, Para-, and Meta-Interactions in Secondary-Alkylphenols from Thermochemical Measurements. *Ber. Bunsenges. Phys. Chem.* **1998**, *102*, 1467−1473.
(25) Gimeno, B.; Martínez, S.; Urieta, J. S.; Pérez, P. Vapor Pressures and Activity Coefficients of (1-Propanol + 1,8-Cineole) at 10 Temperatures Between 278.15 and 323.15 K. *J. Chem. Eng. Data* **2012**, *57*, 3026−3031.
(26) Stejfa, V.; Fulem, M.; Ruzicka, K.; Cervinka, C. Thermodynamic Study of Selected Monoterpenes II. *J. Chem. Thermodyn.* **2014**, *79*, 272−279.
(27) Abdallah, M. A.; Müller, S.; González-de-Castilla, A.; Gurikov, P.; Matias, A. A.; do Rosário-Broze, M.; Fernández, N. Physicochemical Characterization and Simulation of the Solid−Liquid Equilibrium Phase Diagram of Terpene-Based Eutectic Solvent Systems. *Molecules* **2021**, *26*, 1801.
(28) Aparicio, S.; García, B.; Alcalde, R.; Dávila, M. J.; Leal, J. M. PVTx Measurements of the N-Methylpyrrolidone/Methanol Mixed Solvent: Cubic and SAFT EOS Analyses. *J. Phys. Chem. B* **2006**, *110*, 6933−6942.
(29) Aparicio, S.; Alcalde, R.; García, B.; Leal, J. M. High-Pressure Study of the Methylsulfate and Tosylate Imidazolium Ionic Liquids. *J. Phys. Chem. B* **2009**, *113*, 5593−5606.
(30) Benito, C.; Alcalde, R.; Atilhan, M.; Aparicio, S. High-Pressure Properties of Type V Natural Deep Eutectic Solvents: The Case of Menthol:Thymol. *J. Mol. Liq.* **2023**, *376*, No. 121398.
(31) Leron, R. B.; Hill-Wong, D. S.; Li, M. H. Densities of a Deep Eutectic Solvent Based on Choline Chloride and Glycerol and Its Aqueous Mixtures at Elevated Pressures. *Fluid Phase Equilib.* **2012**, *335*, 32−38.
(32) Leron, R. B.; Li, M. H. High-Pressure Volumetric Properties of Choline Chloride-Ethylene Glycol Based Deep Eutectic Solvent and Its Mixtures with Water. *Thermochim. Acta* **2012**, *546*, 54−60.
(33) Crespo, E. A.; Costa, J. M. L.; Palma, A. M.; Soares, B.; Martin, M. C.; Segovia, J. J.; Carvalho, P. J.; Coutinho, J. A. P. Thermodynamic Characterization of Deep Eutectic Solvents at High Pressures. *Fluid Phase Equilib.* **2019**, *500*, No. 112249.
(34) Sas, O. G.; Ivanis, G. R.; Kijevcanin, M. L.; Gonzalez, B.; Dominguez, A.; Radovic, I. R. High-Pressure Densities and Derived Thermodynamic Properties of Deep Eutectic Solvents with Menthol and Saturated Fatty Acids. *J. Chem. Thermodyn.* **2021**, *162*, No. 106578.
(35) Wagner, W.; Pruss, A. The IAPWS Formulation 1995 for the Thermodynamic Properties of Ordinary Water Substance for General and Scientific Use. *J. Chem. Phys. Ref. Data* **2002**, *31*, 387−535.
(36) Span, R.; Wagner, W. Equations of State for Technical Applications. I. Simultaneously Optimized Functional Forms for Nonpolar and Polar Fluids. *Int. J. Thermophys.* **2003**, *24*, 41−109.
(37) Ihmels, E. C.; Gmehling, J. Densities of Toluene, Carbon Dioxide, Carbonyl Sulfide, and Hydrogen Sulfide over a Wide Temperature and Pressure Range in the Sub- and Supercritical State. *Ind. Eng. Chem. Res.* **2001**, *40*, 4470−4477.
(38) Dávila, M. J.; Alcalde, R.; Atilhan, M.; Aparicio, S. PρT Measurements and Derived Properties of Liquid 1-Alkanols. *J. Chem. Thermodyn.* **2012**, *47*, 241−259.
(39) Dávila, M. J.; Aparicio, S.; Alcalde, R.; García, B.; Leal, J. M. On the Properties of 1-Butyl-3-Methylimidazolium Octylsulfate Ionic Liquid. *Green Chem.* **2007**, *9*, 221−232.
(40) Gaciño, F. M.; Regueira, T.; Comuñas, M. J. P.; Lugo, L.; Fernández, J. Density and Isothermal Compressibility for Two Trialkylimidazolium-Based Ionic Liquids at Temperatures from (278 to 398) K and up to 120 MPa. *J. Chem. Thermodyn.* **2015**, *81*, 124−130.
(41) Fandiñó, O.; Pensado, A. S.; Comuñas, M. J. P.; Fernández, J.; et al. Compressed Liquid Densities of Squalane and Pentaerythritol Tetra(2-ethylhexanoate). *J. Chem. Eng. Data* **2005**, *50*, 939−946.
(42) Okuniewski, M.; Pasuszynski, K.; Domanska, U. (Solid + Liquid) Equilibrium Phase Diagrams in Binary Mixtures Containing Terpenes: New Experimental Data and Analysis of Several Modelling Strategies with Modified UNIFAC (Dortmund) and PC-SAFT Equation of State. *Fluid Phase Equilib.* **2016**, *422*, 66−77.
(43) Aparicio, S.; Alcalde, R.; Dávila, M. J.; García, B.; Leal, J. M. Properties of 1,8-Cineole: A Thermophysical and Theoretical Study. *J. Phys. Chem. B* **2007**, *111*, 3167−3177.
(44) Tihic, A.; Kontogeorgis, G. M.; von Solms, N.; Michelsen, M. L. Applications of the Simplified Perturbed-Chain SAFT Equation of State Using an Extended Parameter Table. *Fluid Phase Equilib.* **2006**, *248*, 29−43.
(45) Martínez, L.; Andrade, R.; Birgin, E. G.; Martínez, J. M. PACKMOL: A Package for Building Initial Configurations for Molecular Dynamics Simulations. *J. Comput. Chem.* **2009**, *30*, 2157−2164.
(46) Bittner, J. P.; Huang, L.; Zhang, N.; Kara, S.; Jakobtorweihen, S. Comparison and Validation of Force Fields for Deep Eutectic Solvents in Combination with Water and Alcohol Dehydrogenase. *J. Chem. Theory Comput.* **2021**, *17*, 5322−5341.
(47) Karabin, M.; Stuart, S. J. Simulated Annealing with Adaptive Cooling Rates. *J. Chem. Phys.* **2020**, *153*, 114103.
(48) Bauer, P.; Hess, B.; Lindahl, E. GROMACS 2022 Source Code; Zenodo, 2022. https://doi.org/10.5281/ZENODO.6103835 (accessed Sept 1, 2024).

(49) Huang, J.; Rauscher, S.; Nawrocki, G.; Ran, T.; Feig, M.; De Groot, B. L.; Grubmüller, H.; MacKerell, A. D. CHARMM36m: An Improved Force Field for Folded and Intrinsically Disordered Proteins. *Nat. Methods* **2017**, *14*, 71−73.
(50) Hatcher, E. R.; Guvench, O.; MacKerell, A. D. CHARMM Additive All-Atom Force Field for Acyclic Polyalcohols, Acyclic Carbohydrates, and Inositol. *J. Chem. Theory Comput.* **2009**, *5*, 1315−1327.
(51) Klauda, J. B.; Venable, R. M.; Freites, J. A.; O'Connor, J. W.; Tobias, D. J.; Mondragon-Ramirez, C.; Vorobyov, I.; MacKerell, A. D.; Pastor, R. W. Update of the CHARMM All-Atom Additive Force Field for Lipids: Validation on Six Lipid Types. *J. Phys. Chem. B* **2010**, *114*, 7830−7843.
(52) Malik, A.; Kashyap, H. K. Origin of Structural and Dynamic Heterogeneity in Thymol- and Coumarin-Based Hydrophobic Deep Eutectic Solvents as Revealed by Molecular Dynamics. *Phys. Chem. Chem. Phys.* **2023**, *25*, 19693.
(53) Hess, B.; Bekker, H.; Berendsen, H. J. C.; Fraaije, J. G. E. M. LINCS: A Linear Constraint Solver for Molecular Simulations. *J. Comput. Chem.* **1997**, *18*, 1463−1472.
(54) Bussi, G.; Donadio, D.; Parrinello, M. Canonical Sampling through Velocity Rescaling. *J. Chem. Phys.* **2007**, *126*, No. 014101.
(55) Parrinello, M.; Rahman, A. Polymorphic Transitions in Single Crystals: A New Molecular Dynamics Method. *J. Appl. Phys.* **1981**, *52*, 7182−7190.
(56) Humphrey, W.; Dalke, A.; Schulten, K. VMD Visual Molecular Dynamics. *J. Mol. Graph.* **1996**, *14*, 33−38.
(57) Brehm, M.; Kirchner, B. TRAVIS−A Free Analyzer and Visualizer for Monte Carlo and Molecular Dynamics Trajectories. *J. Chem. Inf. Model.* **2011**, *51*, 2007−2023.
(58) Tariq, M.; Serro, A. P.; Mata, J. L.; Saramago, B.; Esperança, J. M. S. S.; Lopes, J. N. C.; et al. High-Temperature Surface Tension and Density Measurements of 1-Alkyl-3-Methylimidazolium Bistriflamide Ionic Liquids. *Fluid Phase Equilib.* **2010**, *294*, 131−138.
(59) Esperança, J. M. S. S.; Tariq, M.; Pereiro, A. B.; Araujo, J. M. M.; Seddon, K. R.; Rebelo, L. P. N. Anomalous and Not-So-Common Behavior in Common Ionic Liquids and Ionic Liquid-Containing Systems. *Front. Chem.* **2019**, *7*, 450.
(60) Marcus, Y. Internal Pressure of Liquids and Solutions. *Chem. Rev.* **2013**, *113*, 6536−6551.
(61) Van Den Bruinhorst, A.; Costa Gomes, M. Is There Depth to Eutectic Solvents? *Curr. Opin. Green Sustainable Chem.* **2022**, *37*, No. 100659.
(62) Chen, Y.; Yu, Z. Low-Melting Mixture Solvents: Extension of Deep Eutectic Solvents and Ionic Liquids for Broadening Green Solvents and Green Chemistry. *Green Chem. Eng.* **2024**, *5*, 409−417.
(63) Ruß, C.; König, B. Low-Melting Mixtures in Organic Synthesis−An Alternative to Ionic Liquids? *Green Chem.* **2012**, *14*, 2969.
(64) Trenzado, J. L.; Benito, C.; Atilhan, M.; Aparicio, S. Hydrophobic Deep Eutectic Solvents Based on Cineole and Organic Acids. *J. Mol. Liq.* **2023**, *377*, No. 121322.

https://doi.org/10.1021/acs.iecr.5c00116
Ind. Eng. Chem. Res. 2025, 64, 17958−17974